A Metallicity Dependence on the Occurrence of Core-collapse Supernovae

Thallis Pessi[1,2] , Joseph P. Anderson[2,3] , Joseph D. Lyman[4] , Jose L. Prieto[1,3] , Lluís Galbany[5,6] ,
Christopher S. Kochanek[7,8] , Sebastian F. Sánchez[9] , and Hanindyo Kuncarayakti[10,11]

[1] Instituto de Estudios Astrofísicos, Facultad de Ingeniería y Ciencias, Universidad Diego Portales, Av. Ejército Libertador 441, Santiago, Chile
thallis.pessi@mail.udp.cl
[2] European Southern Observatory, Alonso de Córdova 3107, Vitacura, Casilla 19001, Santiago, Chile
[3] Millennium Institute of Astrophysics MAS, Nuncio Monsenor Sotero Sanz 100, Off. 104, Providencia, Santiago, Chile
[4] Department of Physics, University of Warwick, Coventry CV4 7AL, UK
[5] Institute of Space Sciences (ICE, CSIC), Campus UAB, Carrer de Can Magrans, s/n, E-08193 Barcelona, Spain
[6] Institut d'Estudis Espacials de Catalunya (IEEC), E-08034 Barcelona, Spain
[7] Department of Astronomy, The Ohio State University, 140 West 18th Avenue, Columbus, OH 43210, USA
[8] Center for Cosmology and Astroparticle Physics, The Ohio State University, 191 W. Woodruff Avenue, Columbus, OH 43210, USA
[9] Instituto de Astronomía, Universidad Nacional Autónoma de México, A.P. 70-264, C.P. 04510, México, Ciudad de México, Mexico
[10] Tuorla Observatory, Department of Physics and Astronomy, FI-20014 University of Turku, Finland
[11] Finnish Centre for Astronomy with ESO (FINCA), FI-20014 University of Turku, Finland

Abstract

Core-collapse supernovae (CCSNe) are widely accepted to be caused by the explosive death of massive stars with initial masses $\gtrsim 8\ M_\odot$. There is, however, a comparatively poor understanding of how properties of the progenitors —mass, metallicity, multiplicity, rotation, etc.—manifest in the resultant CCSN population. Here, we present a minimally biased sample of nearby CCSNe from the All-Sky Automated Survey for Supernovae survey whose host galaxies were observed with integral-field spectroscopy using MUSE at the Very Large Telescope. This data set allows us to analyze the explosion sites of CCSNe within the context of global star formation properties across the host galaxies. We show that the CCSN explosion site oxygen abundance distribution is offset to lower values than the overall H II region abundance distribution within the host galaxies. We further split the sample at $12 + \log_{10}(\mathrm{O/H}) = 8.6$ dex and show that within the subsample of low-metallicity host galaxies, the CCSNe unbiasedly trace the star formation with respect to oxygen abundance, while for the subsample of higher-metallicity host galaxies, they preferentially occur in lower-abundance star-forming regions. We estimate the occurrence of CCSNe as a function of oxygen abundance per unit star formation and show that there is a strong decrease as abundance increases. Such a strong and quantified metallicity dependence on CCSN production has not been shown before. Finally, we discuss possible explanations for our result and show that each of these has strong implications not only for our understanding of CCSNe and massive star evolution but also for star formation and galaxy evolution.

1. Introduction

Core-collapse supernovae (CCSNe) are generated by the explosive death of massive stars and are important for the formation of new elements and the evolution of galaxies (Woosley & Weaver 1995; Scannapieco et al. 2008; Johnson 2019). Because the delay between star formation (SF) and death for massive stars is relatively short, CCSNe are expected to be associated with the SF regions of galaxies. Indeed, the connection between CCSNe and young and massive stars has been demonstrated by direct progenitor detections and by a large number of previous environment studies (see, e.g., Anderson et al. 2015; Smartt 2015; and references therein). Massive stars produce strong ionizing fluxes that excite the local interstellar medium, producing H II regions. The latter are thus strong tracers of massive SF within galaxies—specifically, Hα emission can be used as a direct tracer of the star formation rate (SFR) within galaxies (e.g., Kennicutt 1998).

A CCSN explosion happens either after the collapse of an ONeMg core for progenitor stars with initial masses ≈8–10 $M_\odot$ (also known as electron-capture SNe, Miyaji et al. 1980; Nomoto et al. 1982), or the collapse of an Fe core for $\gtrsim 10\ M_\odot$ (Bethe et al. 1979; Bethe 1990).[12] Theoretical models and simulations have demonstrated that the mass ranges of stars above these initial values that produce a CCSN explosion (i.e., that do not collapse directly to a black hole) are not continuous, with many regions of "explodability" (see, e.g., Pejcha & Thompson 2015; Sukhbold et al. 2016; Ebinger et al. 2020; Zapartas et al. 2021).

Stellar evolution models and CCSN simulations suggest that black hole formation should be more common at low metallicity (Heger et al. 2003; Eldridge & Tout 2004; Pejcha & Thompson 2015); however, stellar population modeling suggests there is no strong dependence on the CCSN rate with metallicity (e.g., Briel et al. 2022). Previous observational analyses of CCSN production found only small (e.g., Li et al. 2011; Graur et al. 2017; Frohmaier et al. 2021) or no dependence (e.g., Schulze et al. 2021) on metallicity (although

---

[12] Although the exact dividing initial mass remains uncertain.

these previous works used heterogeneous samples and metallicities derived from global galaxy properties).

In this work, we take advantage of a homogeneous CCSN host galaxy sample from the All-Sky Automated Survey for Supernovae (ASAS-SN) survey (Shappee et al. 2014; Holoien et al. 2017a, 2017b, 2017c, 2019; Kochanek et al. 2017; Neumann et al. 2023) and the large field of view and fine spatial resolution of the integral-field spectrograph MUSE (Bacon et al. 2014) to analyze how progenitor metallicity affects CCSN production. Using this sample, in Pessi et al. (2023, Paper I), we analyzed the differences in the local environment of the different CCSN types, and in T. Pessi et al. (2023, in preparation; Paper II) we analyzed the CCSN environments in the context of the properties of all H II regions within their host galaxies. Here, we present the results of comparing the local CCSN environment metallicity to the overall metallicity distributions of the SF regions in their host galaxies and discuss the implications of the metallicity dependence on CCSN occurrence that we find. This Letter is organized as follows: In Section 2 we present our sample and methods and in Section 3 we show the results of comparing the local CCSN environment to the overall SF across their host galaxies. In Section 4 we discuss the implications of these results and in Section 5 the conclusions are summarized.

2. Data and Methods

We analyzed 98 galaxies that hosted 99 CCSNe detected by the ASAS-SN survey (Holoien et al. 2017a, 2017b, 2017c, 2019; Neumann et al. 2023) and were observed by MUSE, mostly in the context of the All-weather MUse Supernova Integral field Nearby Galaxies (AMUSING) survey (Galbany et al. 2016; L. Galbany et al. 2023, in preparation). MUSE has a spatial sampling of $0\rlap{.}{''}2 \times 0\rlap{.}{''}2$, a field of view of 1 arcmin^2 (in Wide-Field Mode), and a mean spectroscopic resolution of $R \sim 3000$ with wide wavelength coverage (480–930 nm), enabling a detailed spectroscopic analysis of all H II regions within the observed galaxies. The CCSN sample was detected by ASAS-SN between 2014 and 2018 and was reported in Holoien et al. (2017a, 2017b, 2019) and Neumann et al. (2023). Using a homogeneous sample from ASAS-SN minimizes biases in host properties because it is an untargeted and almost spectroscopically complete survey (see, e.g., Shappee et al. 2014; Kochanek et al. 2017, for technical details on the survey). A description of the sample selection, data reduction, and calibration is given in Paper I. From the 111 host galaxies in the initial AMUSING/ASAS-SN sample,[13] we selected 78 that hosted Type II SNe (hereafter SNe II) and 21 that hosted stripped-envelope SNe (SESNe, seven SNe IIb, seven SNe Ib, four SN Ic, two SN Ic-BL, and one ambiguous SN Ibc).[14] The CCSN host galaxies are nearby, with luminosity distances of $10 \lesssim D_L(\mathrm{Mpc}) \lesssim 169$.

We characterize the CCSN host galaxies through H II region segmentation by combining the observed Hα signal of adjacent spaxels into one region. We use IFUANAL[15] (Lyman et al. 2018) and the "nearest bin" method to perform the segmentation and obtain emission line and stellar continuum fits for each H II region in addition to that of the SN. Stellar

continuum fitting is performed with STARLIGHT (Cid Fernandes et al. 2005; Mateus et al. 2006), and multiple Gaussians are then fit to the emission lines of the continuum-subtracted spectra.

For each H II region (including that of each CCSN explosion site), the oxygen abundance (hereafter [O/H]—a proxy for metallicity) is estimated following Dopita et al. (2016, D16), using the ratios of [N II]$\lambda6584$ to [S II]$\lambda\lambda6717$, 31 and [N II] $\lambda6584$ to Hα. The D16 index is calibrated using photoionization models and is insensitive to reddening due to the nearby line ratios. It has been shown that D16 removes any dependence on the inferred abundance with ionization (Krühler et al. 2017). In the Appendix, we repeat part of our analysis using the commonly employed O3N2 and N2 diagnostics of Marino et al. (2013). We also extract the Hα flux of each H II region and use the luminosity distance (derived from the CMB frame redshift), the host galaxy extinction correction from the Balmer decrement, and the Galactic reddening correction to estimate the Hα luminosity ($L_{\mathrm{H}\alpha}$) that is converted into an SFR as explained below.

Although the lifetime of a H II region ($\sim$10 Myr, e.g., Tremblin et al. 2014; Xiao et al. 2018) is shorter than the delay time of CCSNe (up to $\sim$200 Myr, when considering binary evolution, e.g., Zapartas et al. 2017; Briel et al. 2022), there should not be a significant abundance evolution in a couple generations of new SF. Therefore, the considered H II regions are a reasonable proxy for the progenitor abundance.

Given that the amount of ionizing radiation per unit SF is a function of metallicity,[16] we use a Binary Population and Spectral Synthesis (BPASS; Eldridge et al. 2017; Stanway & Eldridge 2018) prescription to correct for this effect and obtain SFRs from H II region Hα luminosities. We use a BPASS prescription with binary stellar populations, an initial mass function (IMF) consistent with Kroupa et al. (1993), and an upper mass limit of 300 $M_\odot$, as described in Eldridge et al. (2017).

To characterize the star-forming regions within the galaxies, we examine the cumulative distributions of SFR sorted by [O/H] (for a previous use of this method, see Lyman et al. 2018). For $i = 1 \cdots N$ H II regions with SFR$_i$ and [O/H]^i sorted by the oxygen abundance, we examine the integral distribution

$$\mathrm{SFR}(<[\mathrm{O/H}]_i) = \mathrm{SFR}_{\mathrm{tot}}^{-1} \sum_{j=1}^{i} \mathrm{SFR}_j, \qquad (1)$$

where $\mathrm{SFR}_{\mathrm{tot}} = \sum_i \mathrm{SFR}_i$ is the total SFR of all the H II regions within our sample. This gives the fraction of SF in each region compared to the total SF of the full sample as a function of metallicity.

3. Results

Figure 1 shows the overall cumulative distribution of SFR sorted by [O/H] for the CCSN environments (in red) and for all the 8810 identified H II regions within the galaxies of the sample (in black), as in Equation (1). The shaded regions show 500 bootstrap resamplings of each distribution and the solid lines show the median of the realizations. The resampling is done by adding a Gaussian scatter on the measured errors of

---

[13] https://sites.google.com/view/theamusingasassnsample
[14] We remove all interacting events (IIn, Ibn) given the less clear nature of their progenitors.
[15] https://ifuanal.readthedocs.io/en/latest/index.html

[16] Other effects, such as α-enhancement could affect the ionizing flux as a function of oxygen abundance (e.g., Byrne et al. 2022, although in this work only colder and older stellar atmospheres were altered, with the effect being uncertain for younger stellar populations).
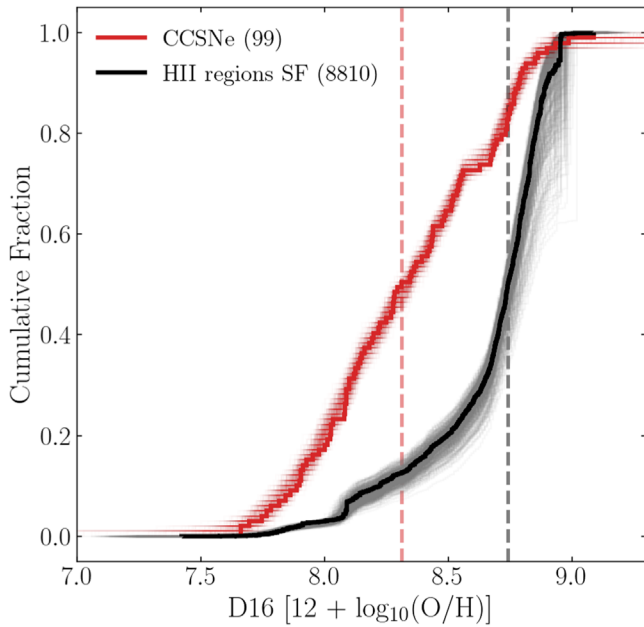
Figure 1. The black line shows the cumulative distribution of SFR sorted by [O/H] for all the H II regions in the galaxies, while the red line shows the cumulative distribution of [O/H] at CCSN sites. The shaded regions show 500 bootstrap resamplings of each distribution (using the errors on the measured parameters) and the solid lines show the median of the realizations. The black and red dashed lines show the median [O/H] of the distributions for the H II regions and CCSNe, respectively.

[O/H] and SFR, with the Gaussians centered at the [O/H] and SFR values, using their uncertainties for the standard deviation. The CCSNe have a median [O/H] ~ 8.30 dex (red dashed line), while the overall SF has a median [O/H] ~ 8.74 dex (black dashed line). This suggests that CCSN production does not follow the metallicity distribution of SF within all galaxies, but it is instead biased toward SF regions with lower abundance.[17]

The gray lines in Figure 2 show the cumulative distributions of SF as a function of [O/H] for all the H II regions within each of the individual 86 CCSN host galaxies from our initial sample. From the initial sample (presented in Figure 1), we could not estimate a $L_{H\alpha}$ for their associated H II region for six CCSNe (SN2018yo, SN2017gbv, ASASSN-17oj, ASASSN-16ba, ASASSN-16al, and SN2015W) due to the low signal-to-noise ratio, so they are excluded from the analyses presented in Figures 2 and 3. We also removed seven CCSNe (SN2015bm, ASASSN-15lv, ASASSN-16gy, ASASSN-18ou, SN2017ewx, SN2017ivu, and SN2016afa) from the initial sample, where only one H II region in the host galaxy was identified. The small markers show the SF fraction rank (i.e., the y-axis position in the cumulative distribution; e.g., Galbany et al. 2016, 2018) and [O/H] of each CCSN environment within each distribution, and the large markers show the median of these values for the CCSNe. A uniform distribution with a median SF fraction of 0.5 would indicate that the SNe do not show any preference for occurring in regions with higher or lower values of [O/H] within their host galaxies. The [O/H] values range from $12 + \log_{10}(O/H) \sim 7.4$ dex to ~ 9.0 dex,

---

[17] If older H II regions had lower oxygen abundances then this could produce some of the effect we observe. However, we do not find a correlation between age, estimated by the Hα EW, and oxygen abundance in our sample. These results will be outlined in Paper II.
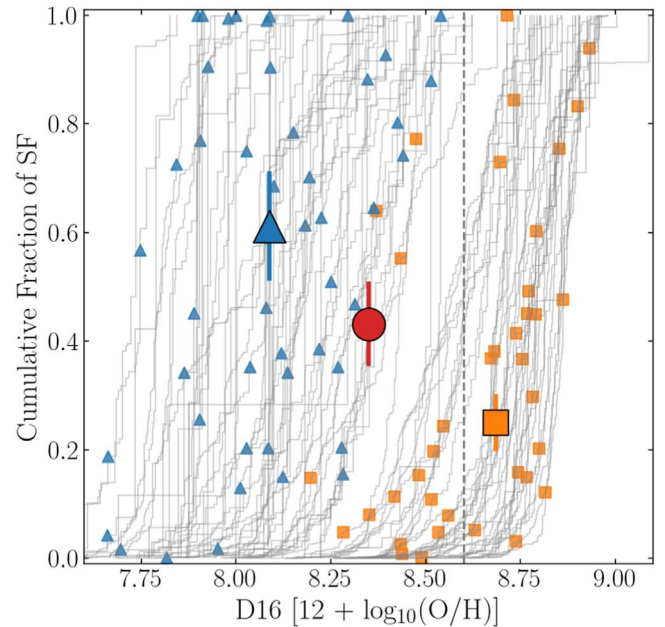

Figure 2. Cumulative distributions of the fraction of SF as a function of [O/H] for H II regions within individual galaxies. Each gray line is the distribution for one galaxy and the small symbols are the SF fraction rank and [O/H] of the CCSN environments within their host galaxy SF distributions. The median rank is given by the big markers, with uncertainties estimated by the median of the 1σ of 500 bootstrap resamplings of each distribution. The blue triangles and orange squares represent the galaxies in which the H II region with the highest [O/H] has a value lower or higher than $12 + \log_{10}(O/H) = 8.6$ dex (indicated by the dashed line), respectively. The red circle shows the median values for the full sample.
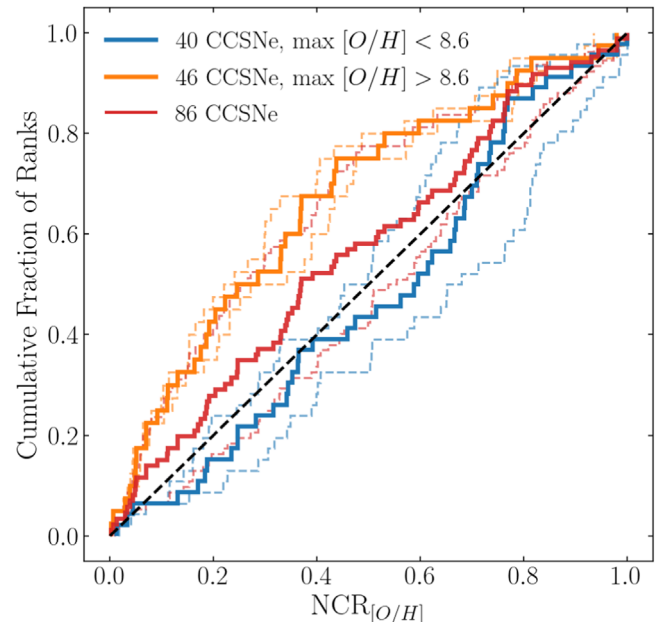

Figure 3. The oxygen abundance NCR for the CCSNe. The red line shows the distribution for the full sample, and the blue and orange lines show, respectively, the galaxies where the largest metallicity value of their H II regions is lower or higher than $12 + \log_{10}(O/H) = 8.6$ dex. An unbiased distribution with respect to metallicity should follow the dashed diagonal line in the plot. The solid lines show the median of 500 bootstrap resamplings of each cumulative distribution and the dashed lines show the 1σ of the realizations.

and the red circle shows the median [O/H] of $12 + \log_{10}(O/H) \sim 8.35$ for the full sample. The median SF fraction of 0.46 ± 0.08 suggests an unbiased production of

CCSNe as a function of metallicity (but see below). The uncertainties of the rank fractions are again estimated using bootstrap resampling.

Next, in Figure 2, we now split the galaxies at $12 + \log_{10}(O/H) = 8.6$ dex (nearly solar; Asplund et al. 2021) based on the H II region in the galaxy with the highest abundance. The blue triangles and orange squares show the SN fraction ranks of these low- and high-abundance galaxies, respectively. The median SF fraction of the CCSNe in the low-metallicity galaxies is 0.61 ± 0.12, but the median SF fraction for the high-metallicity galaxies is 0.24 ± 0.05. Those SNe within higher-metallicity galaxies occur in relatively lower-metallicity regions within their hosts, in contrast to those in the lower-metallicity galaxies.

We analyze the two distributions of SF fraction ranks through the normalized cumulative rank (NCR) of the CCSNe, shown in Figure 3. The NCR is based on the method presented in James & Anderson (2006), but taking the rank of each CCSN in the cumulative fractions of SF as a function of [O/H] for their host galaxies (see Lyman et al. 2018 for a similar application of this method). The x-axis in Figure 3 becomes the SF fraction that is the y-axis in Figure 2. A distribution of SNe that is unbiased with respect to abundance would follow the diagonal (i.e., a uniform distribution of ranks). A distribution biased to higher metallicities will lie below the diagonal and one biased to lower metallicities will lie above it.

The solid lines in Figure 3 show the median of the 500 bootstrap resamplings for the cumulative distributions, while the dashed lines show the 1σ scatter realizations. Figure 3 shows that for the full CCSN sample and the low-metallicity galaxies, the SF fraction distribution follows the diagonal line, suggesting an unbiased dependence of these events with respect to metallicity. The Kolmogorov–Smirnov (KS) test (Chakravarti et al. 1967) between the low-metallicity galaxy distribution and a straight line has a p-value $= 0.69$, suggesting no significant metallicity bias. On the other hand, for higher-metallicity galaxies, the CCSN SF fractions are shifted to the left of the diagonal, with a KS-test p-value $= 0.03$. This suggests that they do not follow the distribution of SF as a function of metallicity in their host galaxies and are biased to SF at lower metallicities.

In Figure 4, we divide the H II regions into seven 0.2 dex wide bins of abundance, and for each bin calculate

$$R_{[O/H],i} = \frac{N_{CCSN,[O/H],i}}{SFR_{tot,[O/H],i}}, \qquad (2)$$

where $N_{[O/H],CCSN,i}$ and $SFR_{tot,[O/H],i} = \sum_i SFR_{[O/H],i}$ are the numbers of CCSN and the total SFR (in units of $M_\odot\,yr^{-1}$) associated with abundance bin i. $R_{[O/H],i}$ is proportional to the occurrence rate of CCSN per unit of SF. Figure 4 also shows "violin" errors from 500 bootstrap resamplings of the distributions. The median values of the resamplings, the 1σ uncertainty, the central abundance, and the number of SNe in each bin are reported in Table 1. Figure 4 also presents a second-order polynomial fit of

$$y = 0.11 - 2.25\,x - 1.17\,x^2 \qquad (3)$$

between $12 + \log_{10}(O/H) = 7.6$ and 9.0 dex, where $y = \log_{10} R_{[O/H]}$ and $x = [O/H] - 8.69$.

Figure 4 shows that the occurrence of CCSNe per unit of SF at lower oxygen abundance appears to be significantly larger
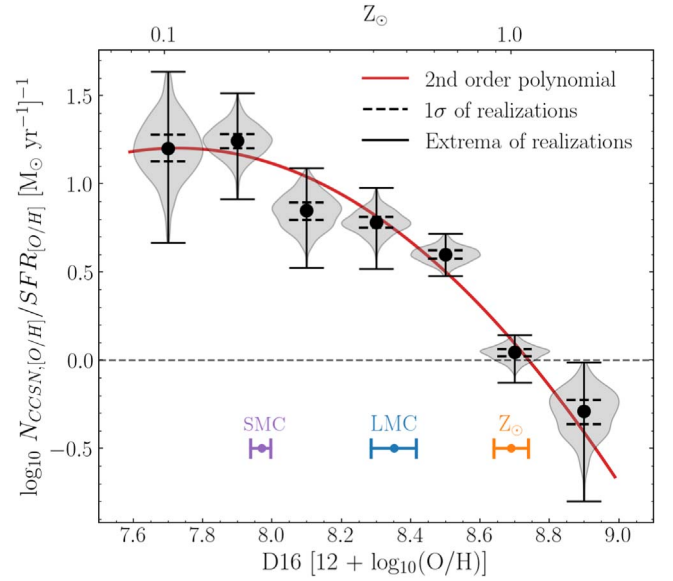

Figure 4. The occurrence of CCSNe per unit of SF as a function of [O/H]. This is estimated by dividing the number of CCSNe, $N_{[O/H],CCSN}$, by the total SFR, $SFR_{tot,[O/H],i}$, over binned intervals in the abundance axis. The violin plots show 500 bootstrap resamplings in each abundance interval of 0.2 dex. The black dots show the median of these realizations, while the dashed and solid lines show, respectively, the 1σ and the extrema of the realizations. We fit a second-order polynomial to the median values, weighting it by the 1σ uncertainties. A horizontal dashed line is shown at $R_{[O/H],i} = 1$. The orange dot shows the abundance for the Sun (Asplund et al. 2021) and the purple and blue dots show the median abundances for, respectively, the small magellanic cloud (SMC) and large magellanic cloud (LMC) (Toribio San Cipriano et al. 2017).

Table 1
The Occurrence Rate of CCSN per Unit of SF, as a Function of Abundance

N_{SN}	$R([O/H])$	1σ	[O/H]
7	15.54	4.94	7.70
12	17.26	3.18	7.90
16	7.01	1.65	8.10
17	6.08	0.82	8.30
20	4.00	0.37	8.50
16	1.09	0.10	8.70
8	0.50	0.10	8.90

than at higher abundances. The occurrence rate declines as metallicity increases, with $R_{[O/H]} \approx 15.5$ at $12 + \log_{10}(O/H) \sim 7.7$ dex and $R_{[O/H]} \approx 0.5$ at $12 + \log_{10}(O/H) \sim 8.9$ dex. The latter value is nearly 25 times lower than the former, showing a large occurrence difference over metallicity. Figure 4 also shows the abundances for the SMC, LMC (Toribio San Cipriano et al. 2017), and the Sun (Asplund et al. 2021). The occurrence of CCSNe per unit SF in abundances close to the SMC and LMC values are higher by factors of ~ 15 and ~ 5 than at abundances close to solar. We show the occurrence of CCSN per unit of SF as a function of two other oxygen abundance indicators in the Appendix, finding consistent results.

4. Discussion

We have found that the CCSN production appears to be strongly dependent on metallicity, with the detected number of CCSNe relative to SF decreasing as oxygen abundances increase. CCSNe do not follow the general distribution of SF

as a function of metallicity and tend to happen within relatively lower-metallicity regions in higher-metallicity galaxies. In lower-metallicity galaxies, the occurrence of CCSNe seems to be unbiased with respect to metallicity. When binning SNe and SF by oxygen abundance, we find a clear decreasing occurrence of CCSNe per unit SF with increasing [O/H].

Previous works have explored the metallicity dependence of the occurrence of long gamma-ray bursts (which are connected to SNe Ic-BL; Fruchter et al. 2006; Stanek et al. 2006, 2007; Kewley et al. 2007; Modjaz et al. 2008; Mannucci et al. 2011; Graham & Fruchter 2013, 2017) and superluminous (SL)SNe (Stoll et al. 2011; Chen et al. 2013, 2017; Lunnan et al. 2013; Frohmaier et al. 2021). Some works also discussed a metallicity effect on the rate of SNe Ia (Sullivan et al. 2006; Li et al. 2011; Graur & Maoz 2013; Kistler et al. 2013; Graur et al. 2017; Brown et al. 2019; Johnson et al. 2022). There are a number of studies on the correlations between CCSN rates and host properties. In particular, Li et al. (2011) found that the CCSN rates per unit luminosity (either B or K band) or stellar mass decreased with galaxy luminosity or mass using the LOSS SN sample (Li et al. 2000; Filippenko et al. 2001). Indeed, the rates dropped by a factor of $\sim$5 between host galaxy stellar masses of $10^9 \, M_\odot$ and $2 \times 10^{10} \, M_\odot$. Graur et al. (2017) reanalyzed those data and found changes in the CCSN rate per unit stellar mass of a factor of $\sim$6 for Type II SN and a factor of $\sim$4 for SESNe between galaxies oxygen abundances of $\sim$8.7 to $\sim$9.2 dex, which is similar to what we see in Figure 4. Graur et al. (2017) argue, however, that this is due to changes in the specific galaxy SFRs rather than metallicity. Frohmaier et al. (2021) also found a drop in the CCSN rates per unit stellar mass of a factor of $\sim$6 between masses of 10^9 and $10^{11} \, M_\odot$. Here, we are directly examining the dependence of the occurrence of CCSN per unit SF as a function of metallicity, and the driver appears to be environment metallicity.

Our study has some significant advantages compared with previous analyses: (1) we use a homogeneous sample of CCSNe detected by ASAS-SN that (2) were selected in a minimally biased way to be observed by MUSE (see Paper I for a more detailed description of sample selection), and (3) we use emission-line spectroscopy of spatially resolved H II regions to measure both metallicities and SFRs across the galaxies (in contrast to central metallicities, taken, e.g., from Sloan Digital Sky Survey, or global galaxy properties derived from photometry).

We now outline possible explanations for the result presented above. It is important to note that while the exact explanation of our result is currently unclear, any of the below possibilities—if confirmed—would have strong implications for our understanding of the CCSN phenomenon and/or massive SF within galaxies.

The first possibility that we discuss is that our findings are the result of selection effects and that we are missing CCSNe within higher-metallicity H II regions. This could be caused by higher extinction in higher-metallicity regions or the difficulty in detecting SNe in high-surface-brightness regions (which are generally of higher metallicity). While we do find that higher-abundance H II regions have slightly higher $E(B - V)$ values than lower regions, this difference is not significant, and neither is the overall distribution of host H II region extinction (see Paper I and Paper II). In addition, near-infrared surveys suggest that only around 20% of CCSNe are likely to be missed in the local Universe due to extinction in optical surveys—this is

much less than required to explain our result (e.g., Fox et al. 2021). It has also been demonstrated that ASAS-SN has a high efficiency in detecting (and classifying) SNe toward the centers —and thus, the most extinction-affected regions—of galaxies (Shappee et al. 2014; Holoien et al. 2017a, 2017b, 2017c, 2019; Kochanek et al. 2017; Neumann et al. 2023). ASAS-SN also found more tidal disruption events per SN than previous surveys, indicating a high efficiency for finding transients close to or at the centers of galaxies (Holoien et al. 2017a, 2017b, 2017c, 2019). Finally, it should be noted that any extinction effect that biases our CCSN distribution must also affect our H II SF distribution. If SNe are being missed due to high extinction, the underlying H II regions could also be missed, thus lessening the impact of extinction in our comparative analysis.

Given that ASAS-SN is a magnitude-limited survey, the number of discovered events scales with their peak luminosity. We have made no completeness correction here and essentially we are assuming that the CCSN luminosity function is not strongly abundance-dependent. If the CCSN peak luminosity were dependent on metallicity, this could affect our results. However, we have shown in Paper I that there is no strong correlation between peak luminosity and oxygen abundance at the location of CCSNe, making this explanation less compelling.

Thus, it seems unlikely that selection effects can explain our results. However, should such selection effects—together with others not considered—be responsible for our results, then this would still be a significant result. Indeed, to reproduce our observed number of CCSNe per unit SF as a function of metallicity (if no intrinsic metallicity difference exists) would require that we are missing more than a factor of 10 CCSNe at solar metallicity (per unit SF) compared to the SMC and lower metallicities (as we show in the Appendix, the result changes little if we use difference abundance estimates). This would mean that currently estimated CCSN rates are hugely underestimated, with a significant impact on our understanding of massive star evolution and death.

A second possibility is that there is a strong metallicity dependence on the IMF. Our analysis assumes that the IMF does not vary with environmental properties such as metallicity. This, however, could be the case: at low metallicity, the shape of the IMF could be such that many more massive stars will explode as CCSNe are produced per unit SF, while at high metallicity the IMF may produce many fewer CCSN progenitors. This scenario was explored by recent studies on the metallicity dependence of the IMF (e.g., Li et al. 2023, although any claimed dependence is much smaller than what would be required here). Such a result would also be significant and have many implications for our current understanding of star formation and galaxy evolution.

Our third possible explanation is that Hα is a significantly biased tracer of massive SF; as explained in Section 2, we used a standard prescription for converting the Hα luminosity into an estimate of the SFR, which gives less SFR per unit Hα luminosity at low metallicity because the model stellar populations produce more ionizing radiation per unit SF. If this dependence could be made weaker or even be reversed, this would help to explain our result. However, this would imply that the real metallicity dependence on the Hα to SFR conversion is much higher than commonly used prescriptions.

Finally, it could be that metallicity is a significant factor regulating the "explodability" of massive stars. This would imply that there are many more massive stars exploding as CCSNe within lower-metallicity environments than at higher metallicity (e.g., solar abundance). This result would have a significant impact on our understanding of stellar evolution, the explosion mechanism of massive stars, and the number of different types of compact remnants. This would go against stellar evolution studies and models that suggest that black hole formation is more common at lower-progenitor metallicities (e.g., Heger et al. 2003; Eldridge & Tout 2004; O'Connor & Ott 2011; Ertl et al. 2016), although the metallicity dependence on the expected outcome of failed SNe has yet not been explored in depth (e.g., Kochanek et al. 2008; Piro 2013). Some studies suggest that the lower mass limit for CCSN decreases as a function of metallicity (for those metallicity ranges probed in the current study; e.g., Eldridge & Tout 2004; Ibeling & Heger 2013), and that metallicity can also affect mass loss and the populations of different SNe (for a recent analysis see, e.g., Aguilera-Dena et al. 2022, 2023). The effect of metallicity could be particularly stronger in binary systems. As demonstrated by Laplace et al. (2020), stripped stars in binaries at lower metallicity could have a higher chance of producing an SN, and Laplace et al. (2021) show that the compactness of binary-stripped stars is lower than single stars, making their explodability higher (for previous studies on the influence of binary systems on the core structure, see, e.g., Langer 1989; Woosley et al. 1993; Vartanyan et al. 2021). Additionally, Klencki et al. (2020) show that envelope stripping is delayed at lower metallicities, resulting in a higher final core mass, although Shenar et al. (2020) demonstrate that binary interactions might not dominate the formation of Wolf–Rayets in low-metallicity environments. This, and the fact that stellar multiplicity might be higher at lower metallicity (which has been shown to be the case for low-mass stars; Badenes et al. 2018), could be at play in producing the effect we see in this work (although no strong evidence exists in the case of massive stars, see, e.g., Sana et al. 2013; Dunstall et al. 2015).

5. Conclusions

We have demonstrated that the observed occurrence of CCSNe shows a strong dependence on environment metallicity. Selection effects would not seem to be able to explain such an effect; if they do, this has strong implications for the estimated rates of CCSNe. Our results also challenge the standard assumptions of a universal IMF and the use of Hα as a tracer of SFR; a deep analysis of how these quantities are affected by local SF properties should be further explored. Finally, our results could be explained by a strong dependence of metallicity on the explosion mechanism of massive stars; this effect has not been addressed in depth in the literature and should be taken into account in future theoretical analyses.

Acknowledgments

Appendix
O3N2 and N2 Indicators

The [S II] line used in the D16 index may be affected by ionization due to supernova remnants in galaxies, making it susceptible to contamination (e.g., Kopsacheili et al. 2020; Cid Fernandes et al. 2021). We therefore estimate the occurrence of CCSN per unit of SF, given by Equation (2), using indicators independent of [S II]. Figure 5 shows the resultant occurrence of CCSN per unit of SF as a function of oxygen abundance given by the O3N2 and N2 indexes, both estimated using the Marino et al. (2013) calibration. The O3N2 index uses the Hα, Hβ, [O III]$\lambda5007$, and [N II]$\lambda6584$ emission lines, while the N2 index uses the line ratio between [N II]$\lambda6584$ and Hα.

Figure 5 shows a similar behavior for the occurrence of CCSNe per unit of SF as shown in Figure 4, declining as metallicity increases. The [O/H] values range between 8.2 and 8.56 dex, and we divide the H II regions between six 0.06 dex bins of abundance. In a similar way to Figure 4, we show "violin" uncertainties from 500 bootstrap resamplings of the distributions, and the 1σ and extrema of the realizations given by, respectively, the dashed and solid lines. We also show a second-order polynomial fit to the two indicators. The O3N2 index is fit with $y = 0.5 - 3.0\,x + 4.0\,x^2$, and the N2 index with $y = 0.7 - 3.9\,x - 4.4\,x^2$, between $12 + \log_{10}(O/H) = 8.2$ and 8.56 dex, where $y = \log_{10} R_{[O/H]}$ and $x = [O/H] - 8.4$. The O3N2 index has $R_{[O/H]} \approx 18$ at $12 + \log_{10}(O/H) \sim 8.2$ dex and $R_{[O/H]} \approx 1.5$ at $12 + \log_{10}(O/H) \sim 8.5$ dex, and the N2 index has $R_{[O/H]} \approx 25$ at $12 + \log_{10}(O/H) \sim 8.2$ dex and $R_{[O/H]} \approx 1.2$ at $12 + \log_{10}(O/H) \sim 8.5$ dex. There are large systematic uncertainties between the different abundance indicators (Kewley & Ellison 2008), which can lead to the quantitative differences seen here. However, the large difference factors seen in the three indicators suggest that the
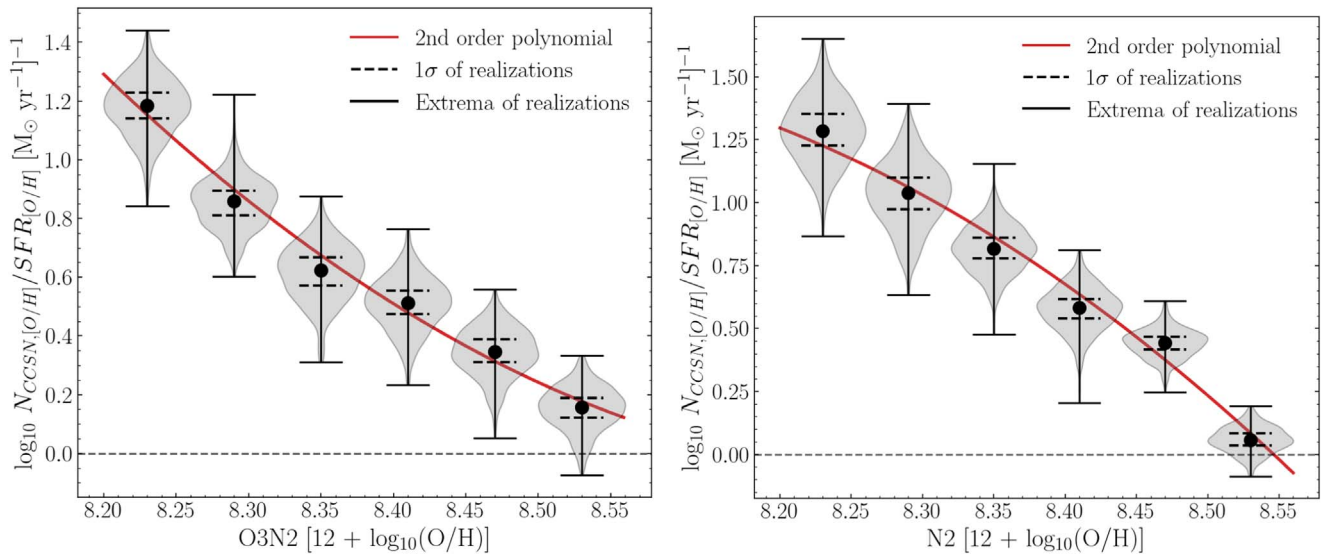
Figure 5. The occurrence rate of CCSNe per unit of SF as a function of [O/H], given by the O3N2 (left panel) and N2 (right panel) indicators. The violin plots show 500 bootstrap resamplings in abundance intervals of 0.06 dex. The black dots show the median of these realizations, and the dashed and solid lines show, respectively, the 1σ and the extrema of the realizations. A second-order polynomial is fit to the median values of each indicator, weighting it by the 1σ uncertainties.

metallicity effect is not affected by these uncertainties. This indicates that the metallicity dependence on CCSN occurrence is independent of the chosen oxygen abundance indicator, being also observed to a similar degree when using O3N2 and N2.

ORCID iDs

Thallis Pessi ⓘ https://orcid.org/0000-0001-6540-0767
Joseph P. Anderson ⓘ https://orcid.org/0000-0003-0227-3451
Joseph D. Lyman ⓘ https://orcid.org/0000-0002-3464-0642
Jose L. Prieto ⓘ https://orcid.org/0000-0003-0943-0026
Lluís Galbany ⓘ https://orcid.org/0000-0002-1296-6887
Christopher S. Kochanek ⓘ https://orcid.org/0000-0001-6017-2961
Sebastian F. Sánchez ⓘ https://orcid.org/0000-0001-6444-9307
Hanindyo Kuncarayakti ⓘ https://orcid.org/0000-0002-1132-1366

References

Aguilera-Dena, D. R., Langer, N., Antoniadis, J., et al. 2022, A&A, 661, A60
Aguilera-Dena, D. R., Müller, B., Antoniadis, J., et al. 2023, A&A, 671, A134
Anderson, J. P., James, P. A., Habergham, S. M., Galbany, L., & Kuncarayakti, H. 2015, PASA, 32, e019
Asplund, M., Amarsi, A. M., & Grevesse, N. 2021, A&A, 653, A141
Astropy Collaboration, Robitaille, T. P., Tollerud, E. J., et al. 2013, A&A, 558, A33
Bacon, R., Vernet, J., Borisova, E., et al. 2014, Msngr, 157, 13
Badenes, C., Mazzola, C., Thompson, T. A., et al. 2018, ApJ, 854, 147
Bethe, H. A. 1990, RvMP, 62, 801
Bethe, H. A., Brown, G. E., Applegate, J., & Lattimer, J. M. 1979, NuPhA, 324, 487
Briel, M. M., Eldridge, J. J., Stanway, E. R., Stevance, H. F., & Chrimes, A. A. 2022, MNRAS, 514, 1315
Brown, J. S., Stanek, K. Z., Holoien, T. W. S., et al. 2019, MNRAS, 484, 3785
Byrne, C. M., Stanway, E. R., Eldridge, J. J., McSwiney, L., & Townsend, O. T. 2022, MNRAS, 512, 5329
Carrick, J., Turnbull, S. J., Lavaux, G., & Hudson, M. J. 2015, MNRAS, 450, 317
Chakravarti, I. M., Laha, R. G., & Roy, J. 1967, Handbook of Methods of Applied Statistics, Vol. 1 (New York: Wiley), 392
Chen, T.-W., Smartt, S. J., Bresolin, F., et al. 2013, ApJL, 763, L28
Chen, T.-W., Smartt, S. J., Yates, R. M., et al. 2017, MNRAS, 470, 3566
Cid Fernandes, R., Carvalho, M. S., Sánchez, S. F., de Amorim, A., & Ruschel-Dutra, D. 2021, MNRAS, 502, 1386
Cid Fernandes, R., Mateus, A., Sodré, L., Stasińska, G., & Gomes, J. M. 2005, MNRAS, 358, 363
Dopita, M. A., Kewley, L. J., Sutherland, R. S., & Nicholls, D. C. 2016, Ap&SS, 361, 61
Dunstall, P. R., Dufton, P. L., Sana, H., et al. 2015, A&A, 580, A93
Ebinger, K., Curtis, S., Ghosh, S., et al. 2020, ApJ, 888, 91
Eldridge, J. J., Stanway, E. R., Xiao, L., et al. 2017, PASA, 34, e058
Eldridge, J. J., & Tout, C. A. 2004, MNRAS, 353, 87
Ertl, T., Janka, H. T., Woosley, S. E., Sukhbold, T., & Ugliano, M. 2016, ApJ, 818, 124
Filippenko, A. V., Li, W. D., Treffers, R. R., & Modjaz, M. 2001, in ASP Conf. Ser. 246, IAU Coll. 183: Small Telescope Astronomy on Global Scales, ed. B. Paczynski, W.-P. Chen, & C. Lemme (San Francisco, CA: ASP), 121
Fox, O. D., Khandrika, H., Rubin, D., et al. 2021, MNRAS, 506, 4199
Freudling, W., Romaniello, M., Bramich, D. M., et al. 2013, A&A, 559, A96
Frohmaier, C., Angus, C. R., Vincenzi, M., et al. 2021, MNRAS, 500, 5142
Fruchter, A. S., Levan, A. J., Strolger, L., et al. 2006, Natur, 441, 463
Galbany, L., Anderson, J. P., Rosales-Ortega, F. F., et al. 2016, MNRAS, 455, 4087
Galbany, L., Anderson, J. P., Sánchez, S. F., et al. 2018, ApJ, 855, 107
Ginsburg, A., Sipőcz, B. M., Brasseur, C. E., et al. 2019, AJ, 157, 98
Graham, J. F., & Fruchter, A. S. 2013, ApJ, 774, 119
Graham, J. F., & Fruchter, A. S. 2017, ApJ, 834, 170
Graur, O., Bianco, F. B., Huang, S., et al. 2017, ApJ, 837, 120
Graur, O., & Maoz, D. 2013, MNRAS, 430, 1746
Heger, A., Fryer, C. L., Woosley, S. E., Langer, N., & Hartmann, D. H. 2003, ApJ, 591, 288
Holoien, T. W. S., Brown, J. S., Stanek, K. Z., et al. 2017a, MNRAS, 467, 1098
Holoien, T. W. S., Brown, J. S., Stanek, K. Z., et al. 2017b, MNRAS, 471, 4966
Holoien, T. W. S., Brown, J. S., Vallely, P. J., et al. 2019, MNRAS, 484, 1899
Holoien, T. W. S., Stanek, K. Z., Kochanek, C. S., et al. 2017c, MNRAS, 464, 2672
Ibeling, D., & Heger, A. 2013, ApJL, 765, L43
James, P. A., & Anderson, J. P. 2006, A&A, 453, 57
Johnson, J. A. 2019, Sci, 363, 474
Johnson, J. W., Kochanek, C. S., & Stanek, K. Z. 2022, arXiv:2210.01818
Kennicutt, R. C., Jr. 1998, ARA&A, 36, 189
Kewley, L. J., Brown, W. R., Geller, M. J., Kenyon, S. J., & Kurtz, M. J. 2007, AJ, 133, 882
Kewley, L. J., & Ellison, S. L. 2008, ApJ, 681, 1183
Kistler, M. D., Stanek, K. Z., Kochanek, C. S., Prieto, J. L., & Thompson, T. A. 2013, ApJ, 770, 88

Klencki, J., Nelemans, G., Istrate, A. G., & Pols, O. 2020, A&A, 638, A55
Kochanek, C. S., Beacom, J. F., Kistler, M. D., et al. 2008, ApJ, 684, 1336
Kochanek, C. S., Shappee, B. J., Stanek, K. Z., et al. 2017, PASP, 129, 104502
Kopsacheili, M., Zezas, A., & Leonidaki, I. 2020, MNRAS, 491, 889
Kroupa, P., Tout, C. A., & Gilmore, G. 1993, MNRAS, 262, 545
Krühler, T., Kuncarayakti, H., Schady, P., et al. 2017, A&A, 602, A85
Langer, N. 1989, A&A, 220, 135
Laplace, E., Götberg, Y., de Mink, S. E., Justham, S., & Farmer, R. 2020, A&A, 637, A6
Laplace, E., Justham, S., Renzo, M., et al. 2021, A&A, 656, A58
Li, J., Liu, C., Zhang, Z.-Y., et al. 2023, Natur, 613, 460
Li, W., Chornock, R., Leaman, J., et al. 2011, MNRAS, 412, 1473
Li, W. D., Filippenko, A. V., Treffers, R. R., et al. 2000, in AIP Conf. Ser. 522, Cosmic Explosions: Tenth AstroPhysics Conf., ed. S. S. Holt & W. W. Zhang (Melville, NY: AIP), 103
Lunnan, R., Chornock, R., Berger, E., et al. 2013, ApJ, 771, 97
Lyman, J. D., Taddia, F., Stritzinger, M. D., et al. 2018, MNRAS, 473, 1359
Mannucci, F., Salvaterra, R., & Campisi, M. A. 2011, MNRAS, 414, 1263
Marino, R. A., Rosales-Ortega, F. F., Sánchez, S. F., et al. 2013, A&A, 559, A114
Mateus, A., Sodré, L., Cid Fernandes, R., et al. 2006, MNRAS, 370, 721
Miyaji, S., Nomoto, K., Yokoi, K., & Sugimoto, D. 1980, PASJ, 32, 303
Modjaz, M., Kewley, L., Kirshner, R. P., et al. 2008, AJ, 135, 1136
Neumann, K. D., Holoien, T. W. S., Kochanek, C. S., et al. 2023, MNRAS, 520, 4356
Nomoto, K., Sparks, W. M., Fesen, R. A., et al. 1982, Natur, 299, 803
O'Connor, E., & Ott, C. D. 2011, ApJ, 730, 70
Pejcha, O., & Thompson, T. A. 2015, ApJ, 801, 90
Pessi, T., Prieto, J. L., Anderson, J. P., et al. 2023, A&A, 677, A28
Piro, A. L. 2013, ApJL, 768, L14
Sana, H., de Koter, A., de Mink, S. E., et al. 2013, A&A, 550, A107
Scannapieco, C., Tissera, P. B., White, S. D. M., & Springel, V. 2008, MNRAS, 389, 1137
Schulze, S., Yaron, O., Sollerman, J., et al. 2021, ApJS, 255, 29
Shappee, B. J., Prieto, J. L., Grupe, D., et al. 2014, ApJ, 788, 48
Shenar, T., Gilkis, A., Vink, J. S., Sana, H., & Sander, A. A. C. 2020, A&A, 634, A79
Smartt, S. J. 2015, PASA, 32, e016
Stanek, K. Z., Dai, X., Prieto, J. L., et al. 2007, ApJL, 654, L21
Stanek, K. Z., Gnedin, O. Y., Beacom, J. F., et al. 2006, AcA, 56, 333
Stanway, E. R., & Eldridge, J. J. 2018, MNRAS, 479, 75
Stoll, R., Prieto, J. L., Stanek, K. Z., et al. 2011, ApJ, 730, 34
Sukhbold, T., Ertl, T., Woosley, S. E., Brown, J. M., & Janka, H. T. 2016, ApJ, 821, 38
Sullivan, M., Le Borgne, D., Pritchet, C. J., et al. 2006, ApJ, 648, 868
Toribio San Cipriano, L., Domínguez-Guzmán, G., Esteban, C., et al. 2017, MNRAS, 467, 3759
Tremblin, P., Anderson, L. D., Didelon, P., et al. 2014, A&A, 568, A4
Vartanyan, D., Laplace, E., Renzo, M., et al. 2021, ApJL, 916, L5
Virtanen, P., Gommers, R., Oliphant, T. E., et al. 2020, NatMe, 17, 261
Weilbacher, P. M., Streicher, O., Urrutia, T., et al. 2014, in ASP Conf. Ser. 485, Astronomical Data Analysis Software and Systems XXIII, ed. N. Manset & P. Forshay (San Francisco, CA: ASP), 451
Woosley, S. E., Langer, N., & Weaver, T. A. 1993, ApJ, 411, 823
Woosley, S. E., & Weaver, T. A. 1995, ApJS, 101, 181
Xiao, L., Stanway, E. R., & Eldridge, J. J. 2018, MNRAS, 477, 904
Zapartas, E., de Mink, S. E., Izzard, R. G., et al. 2017, A&A, 601, A29
Zapartas, E., Renzo, M., Fragos, T., et al. 2021, A&A, 656, L19